I.A.U
Karaj branch

Journal of
A p p l ied
C hemical
R esearch
jacr.kiau.ac.ir

Journal of Applied Chemical Research, 18, 4, 75-98 (2024)

Synthesis of Cu: CuO/WO_3 Nanocomposite as an Effective Photocatalyst for Degradation of Methylene Blue

Marzieh Abdoli[1], Afshin Taghva Manesh[1*], Mehrorang Ghaedi[2], and Mehran Aghaie[3]

[1]*Department of Chemistry, Faculty of Science, Central Tehran Branch, Islamic Azad University, Tehran, Iran*

[2]*Department of Chemistry, Yasouj University, Yasouj 75918-74831, Iran*

[3]*Faculty of Chemistry, North-Tehran Branch, Islamic Azad University, Tehran, Iran*

(Received 12 Feb. 2024; Final revised received 14 May 2024)

Abstract

Cu:CuO/WO_3 nanocomposite was synthesized and characterized by Brunauer Emmett and Teller (BET), Ultraviolet-Visible spectroscopy (UV-Vis), Fourier Transform Infrared Spectroscopy (FT-IR), Field Emission-Scanning Electron Microscopy (FE-SEM), Energy Dispersive X-Ray (EDX), X-Ray Diffraction (XRD) and Diffuse Reflection Spectroscopy (DRS) and consequently applied for methylene blue (MB) photo-degradation. The contribution of various parameters such as initial MB concentration, Cu:CuO/WO_3 content, light exposure time by LED light and pH (main and interaction) on the MB elimination efficiency was studied in the designed reactor. The response surface methodology (RSM) corresponding to the central composite design (CCD) model was used for the Examination of the influence of parameters. MB concentration and the influence of the amount of photo-catalyst on MB degradation reveals that decreasing the amount of photo-catalyst is proportional to diminishing process efficiency. Good agreement between the experimental and the predicted results shows the applicability of the model for effective degradation of MB in aqueous media. According to the predicted and the experimental results in the design of the experiment, Photo-degradation efficiency in optimal conditions of 25 mg of MB, pH = 5, 0.07 g of photo-catalyst over 50 min light exposure, were 99.17 and 99.02%, respectively., while present photo-catalyst is applicable for stable and approximately quantitative degradation of MB over 5 cycles

without significant change in the efficiency. In addition, the kinetic of the process under study follows the quasi-first-order model.

Keywords: Contaminants, Nanocomposites, Cu:CuO/WO_3, Methylene Blue.

Corresponding author: Afshin Taghva Manesh, Department of Chemistry, Faculty of Science, Central Tehran Branch, Islamic Azad University, Tehran, Iran. Email: taaf2007@gmail.com.*

Introduction

Various pollutants, including organic and inorganic species as main sources of water pollution and especially paints as complex organic substances following their arrival to the environment, generate a huge amount of pollutants which as the main aromatic organic structure can absorb visible light over 350-700 nm. Textile industry pollutants following their arrival toward aqueous source media [1-4] and soils owing to their resistance to biodegradation and bioactivity as contaminants generate serious hazards. Their high persistence even in low concentrations is very dangerous for the environment [5-6]. Therefore, the design and application of a safe and economical, absorption and degradation approach is a good candidate to reduce the pollutant contents in environmental media, especially water media for the removal of organic pollutants in wastewater as a highly popular task [7]. Accordingly, several methods including physical, biological and absorption methods suggested as efficient and conventional routes for the removal of water pollutants own their unique merits and drawbacks. Physical methods like flocculation, reverse osmosis and adsorption owing to their non-destructive nature have a low ability to diminish total COD and only transmit organic pollutants to the second phase, which consequently owing to the generation of serious environmental issues assumed more hazardous than the initial stages [8]. Biological aerobic treatment emerged with limitations like the formation of large amounts of sludge and the inability to reduce organic contaminants to desirable levels [9]. The lack of efficiency of conventional treatment methods encourages researchers to design other new processes and search for operating conditions to improve their applicability and efficiency. The advanced oxidation processes (AOPs) are based predominantly on the generation of reactive hydroxyl radicals. AOPs as a good choice based on the utilization of free radicals represent a unique ability to oxidizie organic pollutants to produce non-toxic materials such as water and carbon dioxide [10]. This approach is founded on the application of semiconductor photo-catalysts due to their less toxic nature along with their contribution to wastewater removal, low operating costs and mild and comfortable operation for improving environmental quality. Photo-catalyst selection is based on their sustainability in the environment, cost-effectiveness and achievable in visible light and accordingly classified including metal oxides, sulfides and nitride of metals which are suitable for subset quant degradation of organic pollutants [11-21]. Catalysts based on tungsten derivatives according to their unique properties including high surface-to-volume ratios and quantum effects supply acceptable photo-catalytic function, appropriate for disinfection and renewable energies agents. AOP is an appropriate protocol for the removal of highly degradable and harmful pollutants from drinking water and industrial plant effluents. Catalytic activity was improved by heteroatom doping, enhancing the introduction of active sites and defective edges, improving electron mobility via conjugation, and changing the

electron density in the local carbon atom and speed of the catalytic electron transfer process, which is based on the production of active species including hydroxyl radicals through rapid and non-selective patterns [22, 23]. Irradiation of appropriate lights leads to electron transfer and generation of pores (positive charge) in the ground state, which simultaneously both species causes the formation of radicals suitable for oxidation and reduction of species. Inorganic oxides (IO_4, HSO_5 and S_2O_8) reveal the ability for degradation of para chloro-phenol in the presence and absence of tungsten oxide and a comparison of such results strongly supports the high efficiency of WO_3/IO_4 [24-25]. Then, nano-tungsten oxide shows high efficiency for degradation of the aromatic compounds [26] and Ag_2S/WO_3 applied to the degradation of crystals violet (CV) up to about 98% under visible light [27]. Shi et al. Synthesized Cr/TiO_2 nano-composite and studied it using XRD and XPS techniques. Then, they investigated the nano-composite activity in the degradation of MB dye [28]. Sami et al. synthesized WO3 nanofibers and CuO particles to remove common industrial toxic dyes in wastewater [29]. Samandari et al. synthesized Fe_3O_4@MgAl-LDH nano-catalysts by simultaneous precipitation to remove phenol from wastewater [30]. Farooq et al synthesized Ag–CuO for the degradation of methylene blue... A Varying amount of Ag was doped into CuO to optimize the best catalyst that met the required objectives [45]. Nanostructures based photo-catalyst owing to their unique features like exceptional surface area and the presence of the huge amount of reactive surface centre recommended for degradation of organic pollutants. The present research is devoted to the investigation of MB photocatalytic degradation under visible light irradiation in the presence of Cu: CuO/WO_3 composite. The effect of operational parameters on the degradation efficiency was studied using the response surface methodology approach and subsequently, the optimum point was found using the desirability function. The results of this study can be used in industrial-scale process designing.

Experimental

Materials

Sodium hydroxide (NaOH*)*, Copper (II) chloride ($cucl_2$), Ammonium hydroxide (NH_4OH*)*, Sodium tetra hydro borate ($NaBH_4$), sodium tungsten dehydrate ($Na_2WO_4.2H_2O$*)*, Hydrochloric acid (HCl), Methylene blue ($C_{16}H_{18}N_3SCl$) were all purchased from Merck, Darmstadt, Germany.

Copper(II) chloride ($CuCl_2$), sodium tungsten dehydrated ($Na_2WO_4 \cdot 2H_2O$), ethanol (C_2H_6O), ammonia (NH_3) and sodium boron hydrate ($NaBH_4$), were purchased from Sigma Aldrich Company (American) and were used without any further purification. The solution concentrations were analyzed, using a UV-Vis spectrophotometry (model V-530, Jasco, Japan). The pH Measurements were performed using a pH/redox/temperature meter, model AL20pH

(AQUALYTIC, Germany). X-ray diffraction (XRD, Philips PW 1800) was recorded using Cu Ka radiation (40 kV and 40 mA). The band of samples was estimated based on the diffuse reflectance spectra (DRS) technique using an Avant's spectrophotometer (Avaspec-2048-TEC). The morphologies of the samples were analyzed using scanning electron microscopy (SEM: KYKY-EM3200).

Synthesis of Cu:CuO/WO_3 Nanocomposites

For the synthesis of Cu:CuO/WO_3 photocatalyst, an electrochemical method was used with a voltage of 0 to 5 V and a current density of 10 mA/cm^2 for 1 hour. 4 g of $CuCl_2$ was added in 200 ml of deionized water and 100 ml C_2H_6O for 30 minutes, and then 4 g of $Na_2WO_4 \cdot 2H_2O$ were added. 10 ml of 32% (w/w) NH_3 and 0.5 g of $NaBH_4$ were added to the solution in about 90 minutes. A magnet stirred the electrochemical reactor. The resulting solution was separated by filtration‹, washed several times with distilled water to remove impurities, and dried in an oven at 350 °C.

Results and discussions

FT-IR Analysis

The absorption peaks of FT-IR spectra in the area of 3500-3300 cm^{-1} are declared to the tensile vibrations of water and the peaks observed around 1600 cm^{-1} are related to be the flexural vibrations of water (Figure 1). The absorption peak around 920 cm^{-1}(see Figure 1a.b) has corresponded to the tensile vibrations of W-O. The absorption peak in the 1440 region is related to the tensile vibrations of Cu:CuO as depicted in (Figure 1b) [34], while the absorption band in the 440 cm^{-1} is also recited to the tensile vibrations of CuO. The absorption peak near the 600 cm^{-1} region corresponds to Cu^{2+} - O^{2-} vibrations. The results of the FT-IR method show that the WO_3 and Cu:CuO/WO_3 nanocomposites were successfully synthesized.

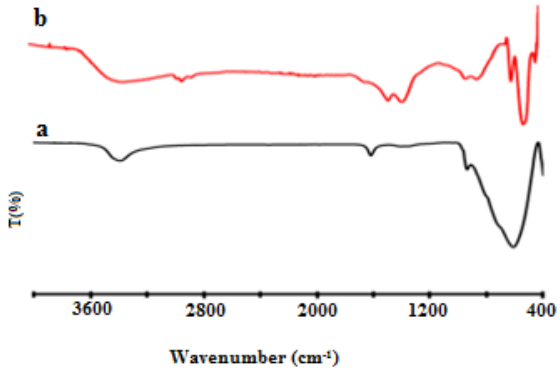

Figure 1. FT-IR spectra of a. WO_3 and b. Cu:CuO/WO_3.

XRD analysis

XRD pattern for the Cu:CuO/WO_3 photocatalyst was recorded in the range of 2θ=10-80 (Figure 2), which is composed of five peaks in 2θ of 26.275, 37.178, 41.786, 56.947 and 50.375 corresponded with the planes (-1 -2 0), (3 0 0), (-2 -2 1), (0 0 2) and (-2 -3 1), which WO_3 corresponds to (JCPDS, NO. 002-0310). The peaks observed in 2θ are 43.473 and 74.679 and declared to the planes (1 1 1) and (2 2 0), respectively, proving the cubic structure of Cu (JCPDS, No. 001-1242). Also, the peaks observed in 2θ of 61.799 and 75.374 correspond to the planes (-1 1 3) and (0 0 4) which represent the monoclinic structure of CuO (JCPDS, No. 002-1041). The peaks indicate that the Cu:CuO/WO_3 nanocomposite is properly fabricated.

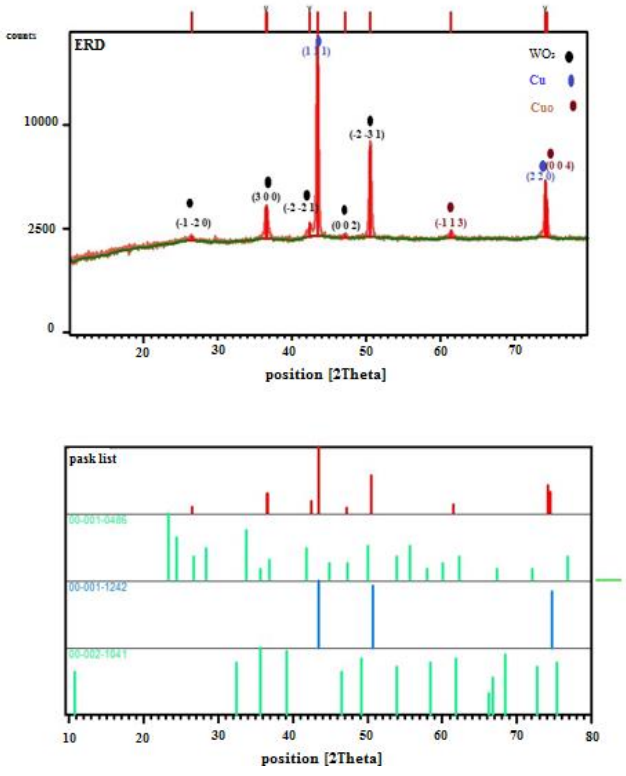

Figure 2. Phase characterization of the nano-catalyst Cu: CuO/WO_3.

FE-SEM analysis

FE-SEM analysis (Figure 3a.b) has been used to investigate the morphology of the photocatalyst surface. The structure of WO_3 nanoparticles is in the form of a plate, and the nanoparticles of Cu and CuO are almost spherical on the plate surface of WO_3. According to the morphology of the surface, the presence of particles with a size in the range of 60-80 nm with a spherical and flat structure has been shown. The EDS spectrum confirms about 73.6% Cu, 13.9% O and 12.5% W (Figure 3c.d).

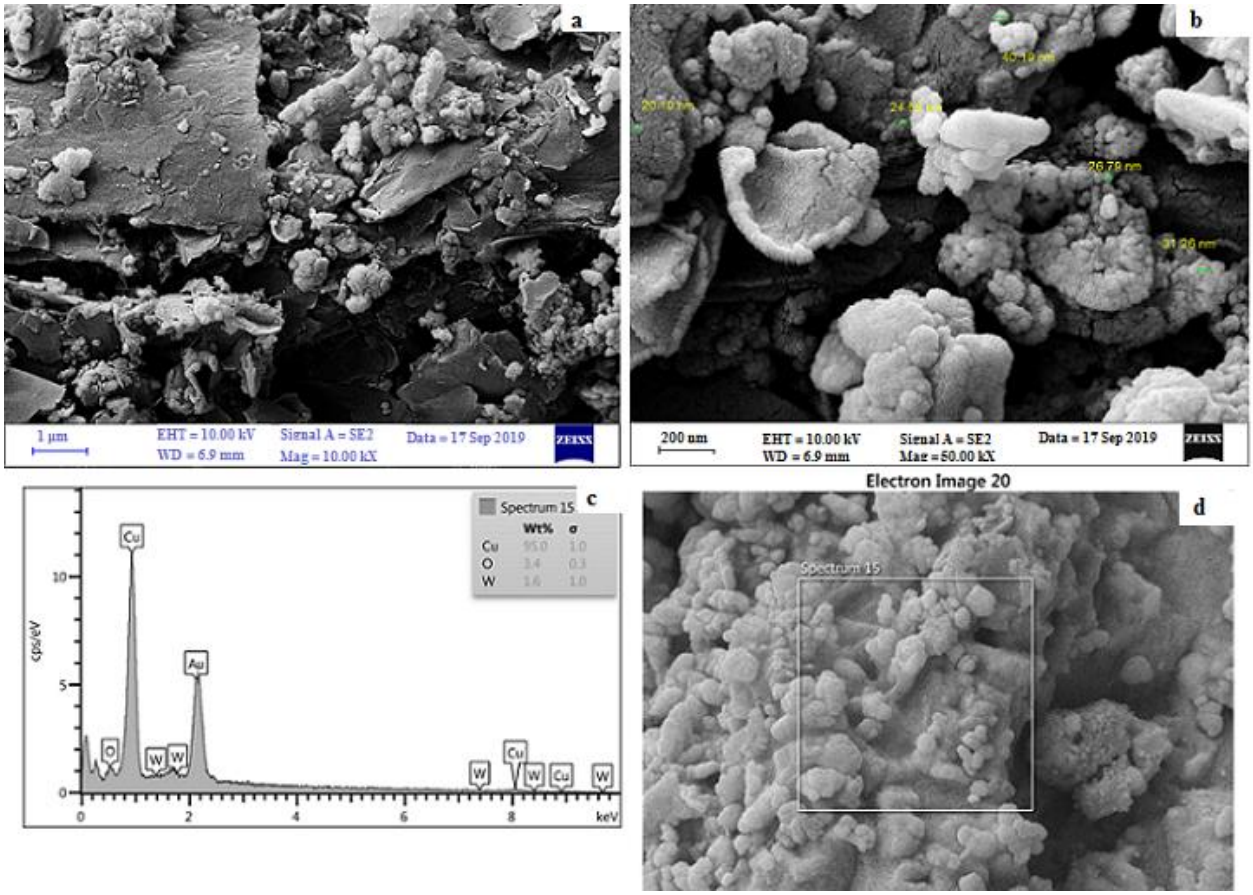

Figure 3. FE-SEM images of Cu:CuO/WO_3nano-composite (a) The scale line is one micrometre and (b) The scale line is 200 nanometers. (C.d) EDS diagram of the Cu:CuO/WO_3 nano-composite.

BET analysis

BET has the unique ability to estimate surface area, type of porosity and approximate diameter of Cu:CuO/WO_3. Figure 4a and the results obtained from the BET analysis show the type IV diagram [35]. Figure 4b shows the estimation of the thickness of the adsorbed layer and the confirmation of the mesoporous structure of the adsorbent. Also, table 1, shows the surface area, diameter of cavities and pore volume obtained from BET [36].

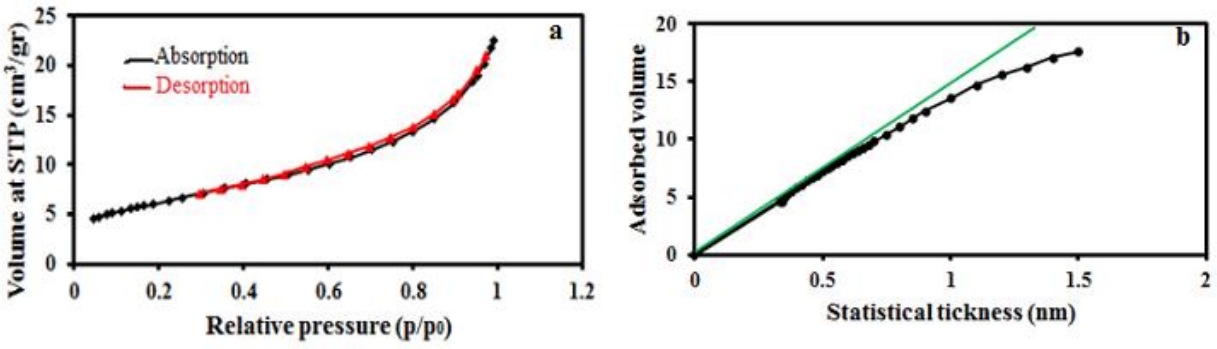

Figure 4. (a) BET adsorption and desorption temperature diagram of Cu:CuO/WO_3 photo-catalytic. (b) BET diagram of Cu:CuO/WO_3 photo-catalytic.

Table 1. The results of Cu:CuO/WO_3 nanocomposite according to Table 1 reveal a porous structure.

Absorption and absorption	**Method**
62.26	**Surface area (m^2.g)**
0.03	**Pore volume (cm^3.g)**
6.2	**diameter of cavities (nm)**

DRS Analysis

Scattered reflection spectroscopy represents the energy gap and absorption edge of the fabricated nanocomposite (Figures 5a and 5c), the photo-catalyst has the maximum absorption intensity in the visible light range with photon energy 2.6 eV and confirms its applicability for the degradation of organic compounds (Figure 5b and 5d).

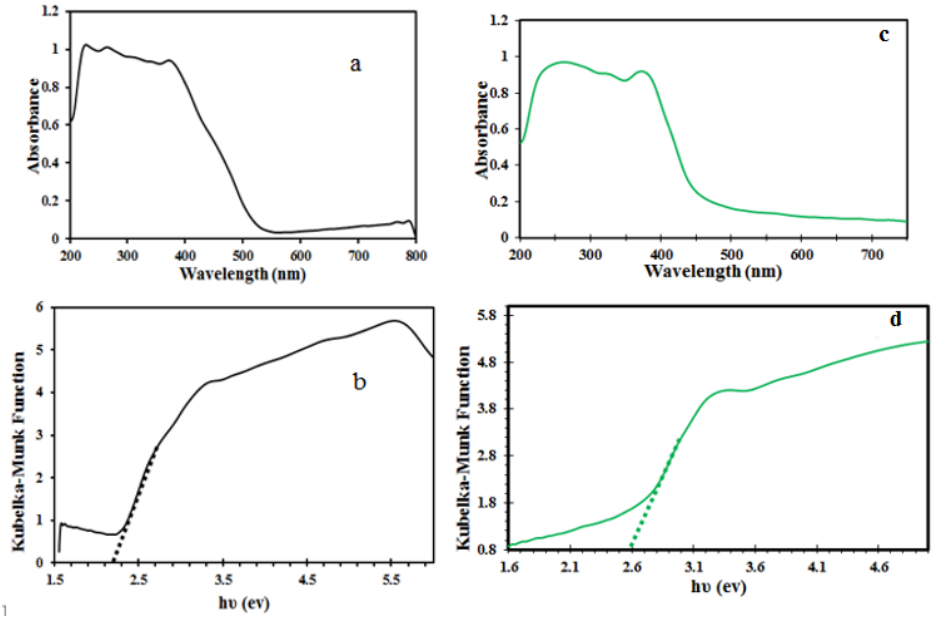

Figure 5. (a) DRS spectrum, (b) Tyuk diagram of WO_3nano-composite.(c) DRS spectrum, (d) Tyuk diagram of Cu: CuO/WO_3 nanocomposite.

MB degradation in the absence of Cu: CuO/WO_3 nano-composite

The degradation of MB by various processes reveals (Figure 6), that after 50 minutes, the MB degradation in the absence of Cu: CuO/WO_3 in the dark was ignored while the presence of photocatalyst and ultrasonic waves denote the highest efficiency for MB degradation.

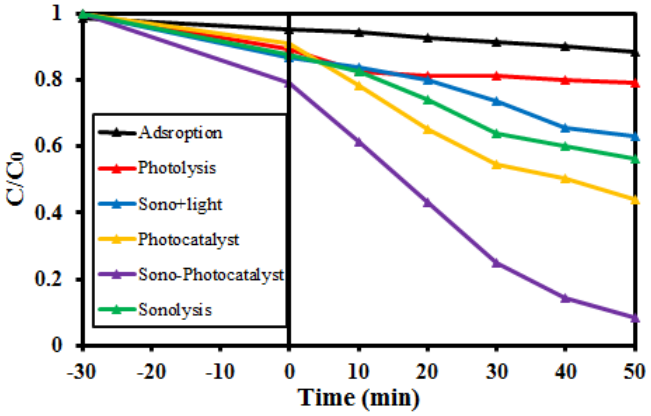

Figure 6. Checking C/C0 by MB color time.

Design

Experimental design based on the expert designers in the format of central composite design (CCD) including 30 experiments composed of 6 central points was conducted to estimate the relation among efficiency of the process with parameters like pH, initial MB concentration, the photo-catalyst mass and irradiation time based on the levels and values selected according to Table 2.

Table 2. CCD matrix of simultaneous photo-degradation of MB with the assistance of Cu: CuO/WO_3.

Factors	Unit	Levels				
		Low (-1)	Central(۰)	High (+1)	-α	+α
A: Catalyst mass	g	0.05	۰,۰۶	۰,۰۷	۰,۰۴	۰,۰۸
B: MB concentration	mg.ml	15.0	۲۰,۰	۲۵,۰	۱۰,۰	۳۰,۰
C:pH	-	5.0	۶,۰	۷,۰	۴,۰	۸,۰
D: Irradiation time	min	۳۰	۴۰	۵۰	۲۰	۶۰

Table 3. Experimental design matrix.

Run	A	B	C	D	Observed	Predicted	Residual
۱	۰۵.۰	۲۵,۰	۵,۰	۳۰	۸۵,۲۴	۸۵,۱	-۰,۱۴
۲	۰,۰۵	۱۵,۰	۵,۰	۳۰	۹۱,۰۷	۹۰,۷	-۰,۳۷
۳	۰,۰۵	۱۵,۰	۵,۰	۵۰	۷۸,۹۸	۷۸,۵	-۰,۴۸
۴	۰,۰۶	۳۰,۰	۶,۰	۴۰	۸۱,۸۰	۸۱,۵	-۰,۷۰
۵	۰,۰۶	۲۰,۰	۶,۰	۴۰	۸۰,۸۵	۸۱,۰	۰,۱۵
۶	۰,۰۸	۲۰,۰	۶,۰	۴۰	۹۲,۴۶	۹۱,۵	-۰,۹۶
۷	۰,۰۵	۲۵,۰	۷,۰	۳۰	۷۴,۷۰	۷۴,۵	-۰,۲۰
۸	۰,۰۶	۲۰,۰	۶,۰	۴۰	۸۱,۸۵	۸۱,۰	۰,۱۵
۹	۰,۰۵	۱۵,۰	۷,۰	۳۰	۹۴,۹۵	۹۵,۳	۰/۳۵
۱۰	۰,۰۷	۲۵,۰	۵,۰	۵۰	۹۹,۱۷	۹۹,۰۲	-۰,۱۵
۱۱	۰,۰۷	۲۵,۰	۷,۰	۳۰	۷۶,۸۳	۷۷,۵	۰,۶۷
۱۲	۰,۰۷	۱۵,۰	۵,۰	۵۰	۷۸,۵۷	۷۹,۰۸	۰,۵۱
۱۳	۰,۰۷	۱۵,۰	۷,۰	۵۰	۸۴,۳۶	۸۴,۷	۰,۳۴
۱۴	۰,۰۷	۱۵,۰	۷,۰	۳۰	۸۷,۱۰	۸۷,۵	۰,۴۰
۱۵	۰,۰۶	۲۰,۰	۶,۰	۴۰	۸۲,۸۵	۸۰,۵	-۰,۳۵
۱۶	۰,۰۷	۲۵,۰	۵,۰	۳۰	۸۴,۶۴	۸۵,۱	۰,۴۶
۱۷	۰,۰۵	۱۵,۰	۷,۰	۵۰	۸۲,۰۳	۸۱,۸۷	-۰,۱۶
۱۸	۰,۰۴	۲۰,۰	۶,۰	۴۰	۹۰,۷۴	۹۱,۲	۰,۴۶
۱۹	۰,۰۶	۲۰,۰	۶,۰	۴۰	۸۰,۸۵	۸۰,۱	-۰,۷۵
۲۰	۰,۰۶	۲۰,۰	۸,۰	۴۰	۷۹,۱۲	۷۸,۰	-۱,۱۲
۲۱	۰,۰۶	۲۰,۰	۶,۰	۶۰	۸۵,۲۰	۸۴,۸	-۰,۴۰
۲۲	۰,۰۶	۲۰,۰	۶,۰	۴۰	۸۳,۸۵	۸۰,۵	-۰,۳۵
۲۳	۰,۰۷	۱۵,۰	۵,۰	۳۰	۸۰,۴۸	۸۰,۰	-۰,۴۸
۲۴	۰,۰۷	۲۵,۰	۷,۰	۵۰	۹۰,۵۳	۹۱,۲	۰,۶۷
۲۵	۰,۰۶	۱۰,۰	۶,۰	۴۰	۸۱,۴۵	۸۱,۶۵	۰,۲۰
۲۶	۰,۰۵	۲۵,۰	۷,۰	۵۰	۷۸,۲۲	۷۸,۹	۰,۶۸
۲۷	۰,۰۶	۲۰,۰	۶,۰	۲۰	۸۳,۵۹	۸۳,۵	-۰,۰۹۳
۲۸	۰,۰۶	۲۰,۰	۶,۰	۴۰	۸۱,۸۲	۸۲,۰	۱,۱۵
۲۹	۰,۰۶	۲۰,۰	۴,۰	۴۰	۸۳,۸۸	۸۰,۵	۰,۶۲
۳۰	۰,۰۵	۲۵,۰	۵,۰	۵۰	۸۹,۶۰	۸۹,۵	-۰,۰۹۶

Evaluation of statistical results of experimental design data

Following optimization, the tests are performed and the response values are used to select the most appropriate model. Table 4 presents some of the squares which are based on the results of the quadratic model and binary interaction of variables to investigate the insignificance of the lack of fit (LOF), which according to the results in the table 5, quadratic model is the best model. In Table 6, the best-proposed model is based on the statistical results of the quadratic model.

Table 4. Sequential model of the sum of squares.

Source	sum of squares	Degrees of freedom	average of squares	F-value	P-value	
Mean vs Total	۲۱۱۶۰۰	۱	۲۱۱۶۰۰			
Linear vs Mean	۴۲,۴۴	۴	۱۰,۶۱	۰,۲۹۲۳	۰,۸۸۰۲	
2FI vs Linear	۶۸۹,۹۰	۶	۱۱۴,۹۸	۱۰,۰۵	۰,۰۰۰۱	
Quadratic vs 2FI	۲۰۸,۸۷	۴	۵۲,۲۲	۹۱,۱۵	۰,۰۰۰۱	Proposed
Cubic vs Quadratic	۵,۶۶	۸	۰,۷۰۸۰	۱,۶۹	۰,۲۵۱۲	Hidden
Residual	۲,۹۳	۷	۰,۴۱۸۴			
Total	۲۱۲۶۰۰	۳۰	۷۰۸۶,۶۵			

Table 5. The proposed model is based on a lack of fit.

Source	sum of squares	Degrees of freedom	average of squares	F-value	P-value	
Linear	۹۰۵,۱۹	۲۰	۴۵,۲۶	۱۰۴,۰۵	۰,۰۰۰۱	
Two-factor interaction	۲۱۵,۲۹	۱۴	۱۵,۳۸	۳۵,۳۵	۰,۰۰۰۵	
Second degree	۶,۴۲	۱۰	۰,۶۴۱۸	۱,۴۸	۰,۳۴۹۷	Proposed
Cubic	۰,۷۵۴۱	۲	۰,۳۷۷۰	۰,۸۶۶۸	۰,۴۷۵۱	Hidden
Net error	۲,۱۸	۵	۰,۴۳۵۰			

Table 6. The proposed models based on statistical results.

Source	The standard deviation	R^2	R^2_{adj}	R^2_{pred}	*PRESS*	
Linear	۶,۰۲	۰,۰۴۴۷	-۰,۱۰۸۲	-۰,۴۶۰۸	۱۳۸۷,۴۹	
Two-factor interaction	۳,۳۸	۰,۷۷۱۰	۰,۶۵۰۵	۰,۶۰۷۴	۳۷۲,۹۲	
Second degree	۰,۷۵۶۹	۰,۹۹۱۰	۰,۹۸۲۵	۰,۹۵۷۸	۴۰,۱۰	Proposed
Cubic	۰,۶۴۶۹	۰,۹۹۶۹	۰,۹۸۷۲	۰,۸۸۲۴	۱۱۱,۷۲	Hidden

Analysis of variance

The results of the analysis of variance (ANOVA) to check data dispersion are shown in Table 7. The non-fit model for MB degradation has an F-value of 1.48, while the F-value for the quadratic model is 117.35. The results show that the non-fitted data is negligible compared to the net value. The quadratic equation conation positive and negative signs, which represent the effect of each expression on the origin and the answer to Equation (1), indicate the effect of other expressions on the model.

$$\%R1=+80.85+0.43A+0.086B-1.19C+0.40D+2.49AB+0.68AC+2.55AD-3.61BC+4.11B-0.21CD+2.69A^2+0.19B^2+0.16C^2+0.89D^2 \quad (1)$$

Table 7. Analysis of variance (ANOVA) for CCD (MB).

Source of variation	Sum of Square	Degree of freedom	Mean square	F-value	P-value	Status	Regression coefficients	
							Factor	Coefficient Estimate
Model	941.21	14	67.23	117.35	< 0.0001	Significant	Intercept	80.85
A	4.45	1	4.45	7.76	0.0138		A	0.43
B	0.18	1	0.18	0.31	0.5849		B	0.086
C	33.92	1	33.92	59.20	< 0.0001		C	-1.19
D	3.90	1	3.90	6.80	0.0198		D	0.40
AB	99.55	1	99.55	173.77	< 0.0001		AB	2.49
AC	7.47	1	7.47	13.03	0.0026		AC	0.68
AD	103.68	1	103.68	180.99	< 0.0001		AD	2.55
BC	208.15	1	208.15	363.34	< 0.0001		BC	-3.61
BD	270.36	1	270.36	471.92	< 0.0001		BD	4.11
CD	0.69	1	0.69	1.21	0.2887		CD	-0.21
A^2	198.06	1	198.06	345.73	< 0.0001		A^2	2.69
B^2	1.03	1	1.03	1.79	0.2007		B^2	0.19
C^2	0.72	1	0.72	1.26	0.2794		C^2	0.16
D^2	21.59	1	21.59	37.69	< 0.0001		D^2	0.85
Residual	8.59	15	0.57					
Lack of Fit	6.42	10	0.64	1.48	0.3497	Not significant		
Pure Error	2.18	5	0.44					
Cor Total	949.81	29						
Quadratic summary statistics		R^2	Adj-R^2	Pred-R^2	Std. Dev.	C.V. %	PRESS	Adequate precision
Response (R% MB)		0.9910	0.9825	0.9578	0.76	0.90	40.10	45.717

The validity of the model was checked by plotting the predicted response from the experimental results and a high R^2 value of 0.9914 confirms its suitability. A graph of the values of the responses predicted by the model in terms of obtained results is seen in Figure 7. This indicates that the parameters under consideration are independent of each other and the model is valid (Figure 8).

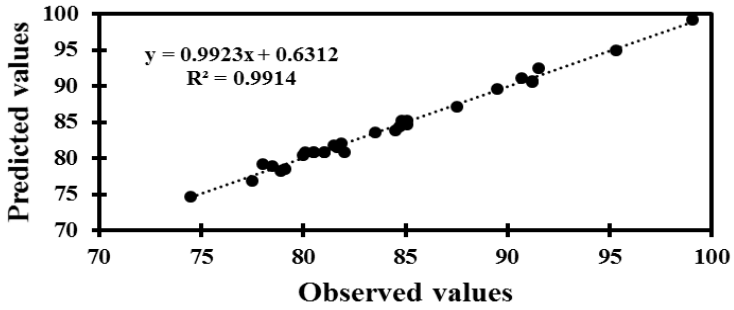

Figure 7. Comparison diagram of P-values and F-values for MB degradation.

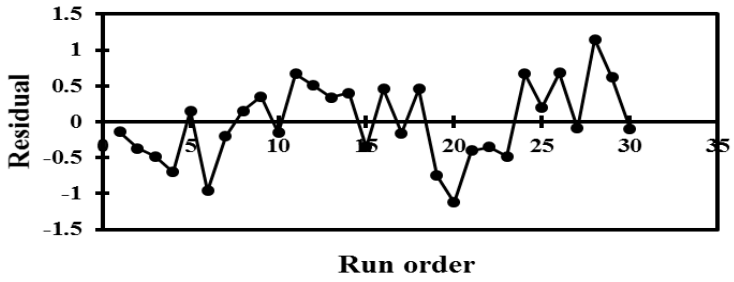

Figure 8. Residual curve.

To further evaluate the model, various statistical parameters such as percentage change coefficient (C.V %) and total squares of prediction error (PRESS) were used. PRESS is an expression of the quality of the model fitting to each point. To obtain this value, first, the first point is removed and the coefficients of the model are calculated. Then the obtained model is used to predict the first point and the difference between these two points is calculated. This process is repeated for each of these points and the sum of the remaining squares is recorded. In this part, the model was also considered in terms of ranking. Table 8 presents the statistical parameters of standard deviation, mean squares, percentage of coefficient of variation, predicted error rate and model accuracy and accordingly based on the value of the predicted error rate, reveals the absence of any systematic error. Also, the balanced R^2 has a lower value and a good match with the coefficient of determination, which indicates significance. It has a model above.

Table 8. Statistical evaluation of the model.

	Response (R%)
Std.Dev	0.76
PRESS	40.10
C. V.%	0.90
R-Squared	0.9910
Adj R-Squared	0.9825
Pred R-Squared	0.9578
Adeq Precision	45.717

Response Surface Design

The response surface methodology (RSM) corresponding to the CCD model was depicted and considered to optimize the critical factors and describe the nature of the response surface in the experiment. The curvature natures of Figure 9 indicate that the response surface plots of removal confirm strong interaction between the variables. Owing to limitations, It is impossible to observe the effect of all parameters on the experimental response (percentage of MB degradation), and therefore the response levels for two parameters are plotted against the experimental response. Information can be obtained by examining the curves of the response levels and the results obtained must be interpreted accordingly.

Examination of the influence of parameters, MB concentration and the amount of photo-catalyst on MB degradation (Figure 9a) reveal that decreasing the amount of photo-catalyst is proportional to diminishing process efficiency. Reversely, increasing the MB content also leads to a lowering decomposition percentage due to an imbalance between the amount of photo-catalyst and MB content. Figure 9b displays the contribution of photo-catalyst and pH on MB degradation. The pH through various mechanisms, ion hydrogen and electrostatic bonding and bipolar and ionic interaction solely or simultaneously contribute to the MB accumulation onto the surface and reactive centre of the photo-catalyst. Increasing the pH increases the photo-catalyst load and thus affects the species transfer. The formation of an electrostatic bond prevents species transfer and thus reduces the percentage of degradation. Protons are rapidly absorbed by cationic dyes and this is thought to prevent the MB accumulation on the photo-catalyst which owing to the cationic nature of MB leads to a reduction in its degradation with increasing pH and the highest photo-degradation efficiency was observed at pH = 5. Figure 9c also displays the result of ultrasound power and exposure time along with photo-catalyst content in percentage. As shown in Figure 9, the most process efficiency has occurred following ultrasound exposure for 30 minutes which expected that immersion of the photo-catalyst in the solution is associated with increasing the migration and

propagation of MB onto the external surface of the photo-catalyst. Raising photo-catalyst content leads to higher MB photo-degradation. Figure 9d describes the impact of pH and MB initial concentration on current protocol efficiency. As can be seen, increasing pH and MB concentration lead to a diminishing in MB, degradation, while decreasing pH and MB concentration is associated with raising the amount of MB degradation. The effect of ultrasound time and initial MB concentration (Figure 9f) reveal that increasing ultrasound time and MB concentration simultaneously lead to higher MB concentration.

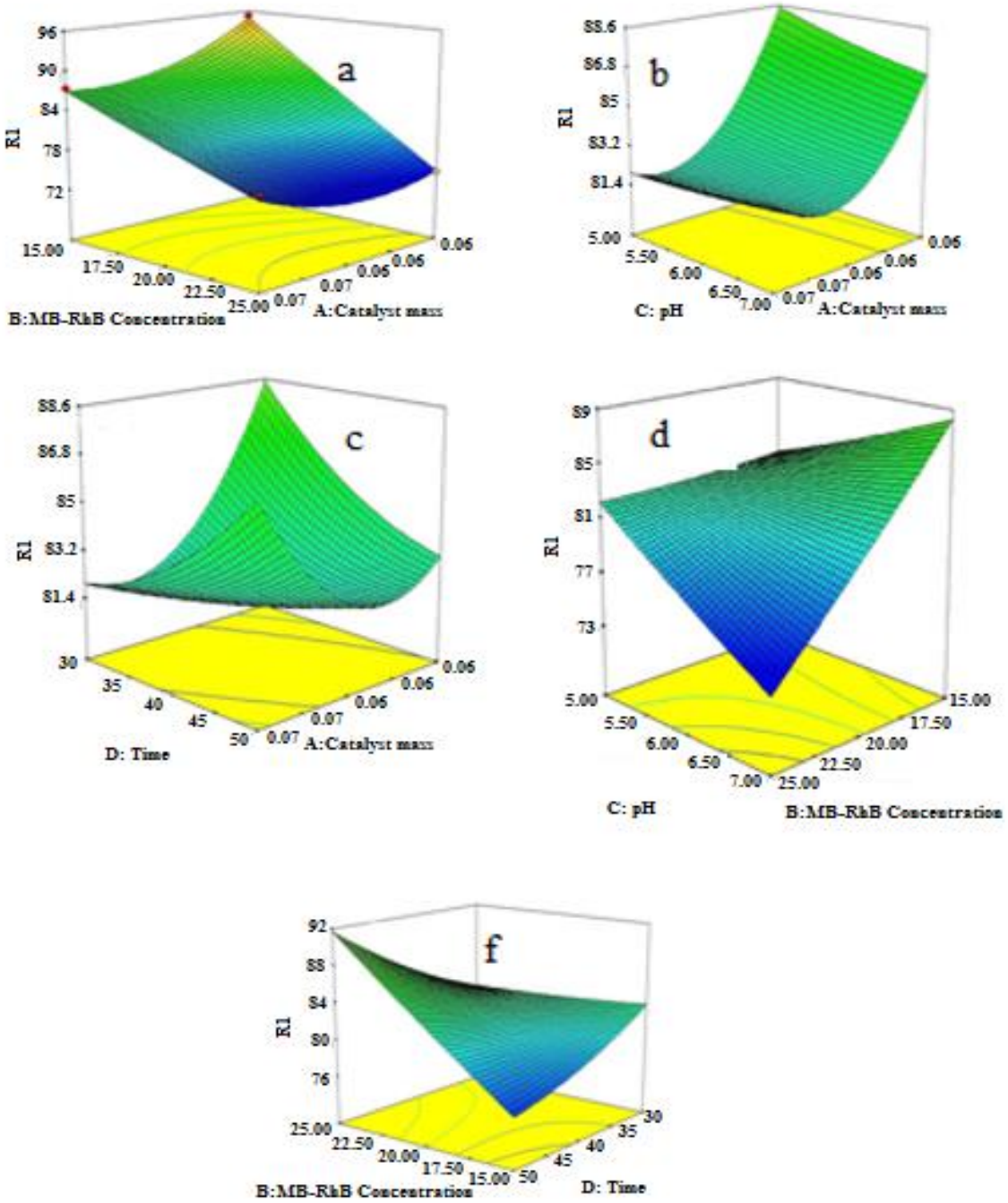

Figure 9. Response levels are related to different parameters.

Optimizing Factors Influencing Percentage of MB photo-degradation

The most important factors in the MB degradation process lead to the achievement of the highest efficiency. The optimal conditions were gained by the appropriate selection of certain levels of effective input parameters. These conditions reflect the effect of different conditions on the response to find optimal values of each variable. According to the prediction, the best results are assigned to adjustment of conditions as is 25 mg L^{-1} of MB following sonication at the pH = 5 in the presence of 0.07 g Cu:CuO/WO_3, which leads to photo-degradation of more than 99.57%.

Investigation of the number of recovery times of Cu: CuO/WO_3 photo-catalyst

One of the effective parameters in determining the efficiency of a photo-catalyst is the possibility of its recovery and reuse. The degradation process of 5 ml of MB with a concentration of 25 mg/ml in the presence of 0.07 g of Cu: CuO/WO_3 photo-catalyst at pH = 5 and a time of 50 minutes was investigated. The results of photo-catalyst recovery are shown in Figure 10. As shown in the figure, the ability to destroy this contaminant with a concentration of 25 mg/ml after 5 times of recovery and reuse is about 86%.

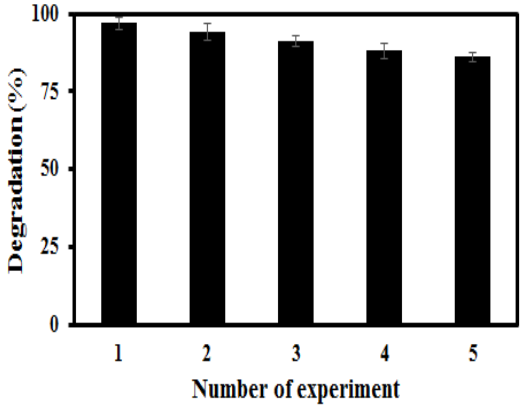

Figure 10. Analysis of nanocomposites in reuse for MB degradation.

The traditional model

A series of similar experiments were performed under adjusted conditions for MB photo-degradation. By comparing the corresponding kinetic curves (first and second-order) based on their correlation coefficient accordingly, the applicability of each of the equations is justified and consequently, their rate constant was calculated. In this regard, the kinetic models of quadratic, Elovich and intermolecular kinetics models were used to investigate the rate of degradation and judgments based on their corresponding constants are gathered in Table 2. According to the coefficients of determination and matching of the data with the kinetic models, it is concluded that MB photo-degradation by Cu: CuO/WO_3-NCs catalyst follows inter-molecular diffusion.

Based on the results of Table 3 and the simulation of kinetic models, it can be said that the kinetics of the dye degradation process in the photo-catalyst follow the phenomenon of intermolecular diffusion and the Langmuir–Hinshelwood (L-H) model [31-33].

$$ln\left(\frac{C_0}{C_t}\right) = kt \qquad (2)$$

Then the In(C_0 / C_t) in terms of different exposure times was investigated (C_0 is the initial dye concentration and C_t is the dye concentration at time t). Figure 11a shows the ln (C_0 / C_t) curve in terms of time. The value of velocity constant k was obtained from the slope of the curve 0.1132. Also, the results of the optical decomposition of MB by Cu: CuO/WO_3 under visible light (blue) radiation justifies the appropriate efficiency of the (L-H) model. The coating surface area (θ) is proportionate to the solid-liquid, Cu:CuO/WO_3 reaction with MB and explained by the L-H model:

$$R = k_r\theta = k_r\frac{KC_0}{1 + KC_0 + K_sC_s} \qquad (3)$$

k_r is the photo-catalytic process rate constants and K_s and K are the solvent and dye absorption coefficients, respectively. C_o and C_s are the initial concentrations of solute and solvent at t = 0. The removal kinetics of many pollutants is analyzed using the Langmuir–Hinshelwood synthetic model, and this model is used to express the relationship between the initial decomposition rate and the concentration of the pollutant. The equation used in the L–H model is as follows:

$$\frac{1}{R} = \frac{1}{k_rK_AC_o} + \frac{1}{k_r} \qquad (4)$$

The K_A parameter is defined by the following equation:

$$K_A=K/(1+K_SC_S) \qquad (5)$$

The 1/R diagram in terms of $1/C_0$ is shown in Figure 11b. The width of the equation is equal to $1/k_r$ and the slope is equal to $1/k_rk_A$. The value of k_r was 0.0114 L/mg and the value of k_A was 87.7 mg/L.

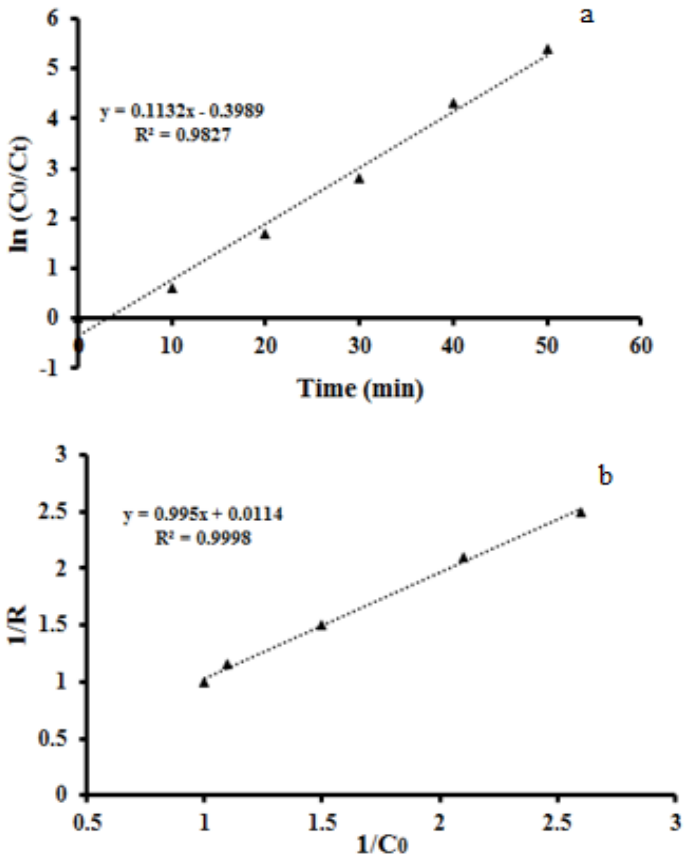

Figure 11. L-H diagram (a) Graph ln (C_0/C_t) in terms of time and (b) Graph 1/R in terms of $1/C_0$.

Mechanism of Cu: CuO/WO_3

In semiconductors, the distance between the conduction band and the capacitance band is such that when a certain amount of energy is received, the electron is transferred from the capacitance band to the conduction band, and by transferring the electron, a positively charged hole is created on the capacitance band. The mechanism of action of the manufactured photo-catalyst (Cu: CuO/WO_3) is shown in Figure 12. As shown in Figure 12, photons of visible radiation are absorbed by WO_3, producing holes and electrons. The electron produced by light is transferred to Cu because it has a higher electron density than CuO, which reduces the probability of combining electron holes. The electrons in Cu can be transferred to CuO, and eventually, the electrons are transferred to oxygen and water is produced [37]. Research has shown that the degradation of organic compounds was done in the presence of various species such as cavities, $OH^{\cdot}$, $O_2^{\cdot}$ and HO_2. In the synthesized photo-catalyst, it seems unlikely that $O_2^{\cdot}$ and HO_2 species cause oxidation of the species (MB dye), because in the Cu: CuO/WO_3 photo-catalyst, the conduction band WO_3 (+ 0.5V relative to NHE) is more positive than the single electron reduction potential of oxygen, it indicates that these species

cannot be processed. Cu: CuO/WO_3 Photocatalytic, (E^o ($O_2.O_2^{\cdot}$) = 20.33 V vs. NHE)) and ((E^o)$O_2.HO_2^{\cdot}$) = 20.55 V vs. NHE) on the other hand, $OH^{\cdot}$ is rarely possible during the photo-catalytic reaction of Cu: CuO/WO_3, so in this mechanism, there are holes created with high oxidation potential (+ 3V relative to NHE) [38] that react with organic compounds and inert compounds such as water. They produce carbon dioxide and other products.

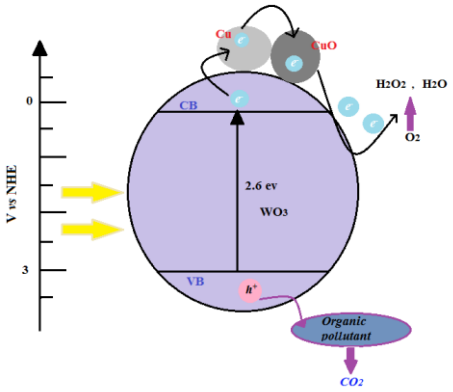

Figure 12. Mechanism of action of Cu: CuO/WO_3 photo-catalyst.

Comparisons with literature

In the end, the results obtained from this article were compared with the results of other articles, which are collected in Table 9.

Table 9. Results of comparison of MB degradation percentage with different nanocomposites.

Reference	time	PH	MB Degradation (%)	synthesis approach	Nano-composite
[39]	۱۸۰ (min)	natural	۱۰۰	solvothermal	MnFe2O4-GSC
[40]	4 (h)	۱۱	۹۵,۲	template synthesis method	THNF nanofibers
[41]	۳۰۰ (min)	5	۸۶,۸۷	hydrothermal	Titanium dioxide nanotubes (TNTs)
[42]	۶۰ (min)	neutral	۹۸	solvothermal	The GO-CS@Cu3(BTC)2
[43]	۳۰ (min)	۱۳,۲	۹۱,۳	Hummers–Offeman method	rGO/TiO_2
[44]	۱۸۰ (min)	۲	۹۲	low-cost sol–gel	2%Fe–ZnO
Current work	۵۰ (min)	۵	۹۹,۲	electrochemical	$Cu:CuO/WO_3$

Table 9 shows that the photocatalyst synthesized in this paper increases the percentage of MB degradation in less time in comparison with similar works.

Conclusion

Cu: CuO/WO_3 nanocomposite for photodegradation of MB was synthesized by the electrochemical process. A CCD investigation reveals that the best optimal conditions are as follows: 0.07 g of Cu: CuO/WO3, 25.0 mg/ml of MB at pH = 5 following 50 minutes of sonication, degradation 99.2% of MB, while the current photocatalyst is applicable. The reaction kinetics follows the quasi-first type and the proposed kinetic models confirms radicals and holes simultaneously and act as a full ingredient for photo-degradation of MB, it produces carbon dioxide and other less harmless compounds.

Acknowledgements

We appreciate the provided supports by the Department of Chemistry of the Central Tehran Branch of Islamic Azad University.

Conflict of interest

The authors have no conflict of interest.

Reference

1. Andreozzi R, Caprio V, Marotta R, Radovnikovic A. Ozonation and H2O2.UV treatment of clofibric acid in water. Hazard Mater. 2003;103:233–246. (A kinetic investigation).

2. Ternes AT, Stuber J, Herrmann N, McDowell Ried D, Kampmann AM. Ozonation: A tool for removal of pharmaceuticals, contrast media and musk fragrances from wastewater. Water Res. 2003;37:1976–1982.

3. Buffle MO, Schumacher JE, Salhi M, Jekel U. vonGunten, Measurement of the initial phase of ozone decomposition in water and wastewater by means of a continuous quench flow system Application to disinfection and pharmaceutical oxidation. Water Res. 2006;40:1884–1894.

4. Doll TE, Frimmel FH. Kinetic study of photocatalytic degradation of carbamazepine, clofibric acid, iomeprol and iopromide assisted by different TiO2 materials determination of intermediates and reaction pathways. Water Res. 2004;38:955–964.

5. Halling Sorensen B, Nielsen SN, Lanzky PF, Ingerslev F, LutzhoftHolten HC, Jorgensen SE. Occurrence, fate and effects of pharmaceutical substances in the environment a review. Chemosphere. 1998;40:357–393.

6. Chatzitakis A, Berberidou C, Paspaltsis I, Kyriakou G, Sklaviadis T, Poulios I. Photocatalytic degradation and drug activity reduction of chloramphenicol. Water Res. 2008;42:386–394.

7. Bokhale NB, Bomble SD, Dalbhanjan RR, Mahale DD, Hinge SP, Banerjee BS, Mohod AV, Gogate PR. Sonocatalytic and sonophotocatalytic degradation of rhodamine 6G containing wastewaters. UltrasonSonochem.2014;21:1797–1804.

8. Ameta R, Benjamin S, Ameta A. Ameta, SC.Photocatalytic degradation of organic pollutants: a review. Mater Sci Forum. 2013;734:247–272.

9. Lam SM, Sin JC, Abdullah AZ, Mohamed AR. Degradation of wastewaters containing organic dyes photocatalysed by zinc oxide: a review. Desalin Water Treat. 2012;41:131–169.

10. Pang YL, Abdullah AZ, Bhatia S. mmReview on sonochemical methods in the presence of catalysts and chemical additives for treatment of organic pollutants in wastewater. Desalination. 2011;277:1–14.

11. Theerthagiri J, Senthil RA, Priya A, Madhavan J, Michael RJV, Ashokkumar M. Photocatalytic and photoelectrochemical studies of visible-light active α-Fe2O3–g-C3N4 nanocomposites. RSC Adv. 2014;4:38222–38229.

12. Kohtani S, Kamoi Y, Yoshioka E, Miyabe H. Kinetic study on photocatalytic hydrogenation of acetophenone derivatives on titanium dioxide. CatalSci Technol. 2014;4: 1084–1091.

13. Zhu LP, Bing NC, Yang DD, Yang Y, Liao GH, Wang LJ. Synthesis and photocatalytic properties of core–shell structured α-Fe2O3@SnO2 shuttle-like nanocomposites. CrystEng Comm. 2011;13:4486–4490.

14. Khedr MH, Halim KS, Soliman NK. Synthesis and photocatalytic activity of nano-sized iron oxides. Mater Lett. 2009;63:598–601.

15. Wang M, Xie F, Chena M, Zhao Y. Preparation of various kinds of copper sulfidesin a facile way and the enhanced catalytic activity by visible light. Mater Chem A. 2013;1:8616–8621.

16. Guan XH, Qu P, Guan X, Wang GS. Hydrothermal synthesis of hierarchical CuS.ZnS nanocomposites and their photocatalytic and microwave absorption properties. RSC Adv. 2014;4:15579–15585.

17. Zhang K, Guo L. Metal sulphide semiconductors for photocatalytic hydrogen production. CatalSci Technol. 2013;3:1672–1690.

18. Du Y, Zhao L, Zhang Y. Roles of TaON and Ta3N5 in the visible-Fenton-like degradation of atrazine. Hazard Mater. 2014;267:55–61.

19. Gaya UI, Abdullah AH. Heterogeneous photocatalytic degradation of organic contaminants over titanium dioxide: a review of fundamentals, progress and problems. PhotochemPhotobiol C. 2008;9:1–12.

20. Theerthagiri J, Senthil RA, Priya A, Madhavan J, Ashokkumar M. Synthesis of a visible-light active V2O5–g-C3N4 heterojunction as an efficient photocatalytic and photoelectrochemical material. New J Chem. 2014;39:1367–1374.

21. Nakamura R, Tanaka T, Nakato Y. Oxygen photoevolution on a tantalum oxynitridephotocatalyst under visible-light irradiation: How does water photooxidation proceed on a metal-oxynitridesurface. PhysChem B. 2005;109:8920–8927.

22. Saien J, Soleymani AR. Degradation and mineralization of Direct Blue 71 in a circulating upflow reactor by UV/TiO_2 process and employing a new method in kinetic study. Hazard Mater. 2007;144:506–512.

23. Berberidou C, Pouliso I, Xekoukoulotakis NP, Mantavirinos D. Sonolytic, photocatalytic and sonophotocatalytic degradation of malachite green in aqueous solutions. Applied Catalysis B: Environmental. 2007;74:63-72.

24. Nambi AB, Anusha JV, Subramanian E. In Situ and Ex Situ Immobilization of Nano Gold Particles in Zeolite Framework and a Comparison of Their Photocatalytic Activities. Inorganic and Organometallic Polymers and Materials. 2018;6:15-26.

25. Kim H, Yoo HY, Hong S, Lee S, Lee S, Park BS, Park H, Lee C, Lee J. Effects of inorganic oxidants on kinetics and mechanisms of WO_3-mediated photocatalytic degradation. Applied Catalysis B: Environmental. 2015;162:515–523.

26. Aslama M, Ismaila IMI, Chandrasekarana S, Hameeda A. Morphology controlled bulk synthesis of disc-shaped WO_3 powder and evaluation of its photocatalytic activity for the degradation of phenols. Hazard Mater. 2014;276:120–128.

27. Abdoli M, Taghva Manesh A, Ghaedi A, Aghaie M. Synthesis and Characterization of Photo-catalyst Ag_2S/WO_3 and its Application for Crystal Violet Degradation in the Aqueous Medium. Chemistry Select. 2022;202103439.

28. Shi Y, Li J, Wang X, Chen X, Yu Z. Photocatalytic decomposition of methylene blue by Cr/TiO2 composite coatings. Surface Engineering.2020;No:1-10.

29. Sami D, Suna N, Ismail CK, Gulcihan GK, Volkan K, Hasan A. Production of CuO–WO_3 hybrids and their dye removal capacity/performance from wastewater by adsorption/photocatalysis. Journal of Water Process Engineering. August 2020, 101390

30. Samandari M, Taghvamanesh A, Hosseini SA, Mansouri S. Magnetic MgAl-LDH: a green nanocatalyst for wet peroxide oxidation of phenol: experimental study and process modeling by response surface methodology and artificial neural network. Desalination Publications. 2021;228:217–228.

31. Heredia JBD, Torregrosa J, Dominguez JR, Peres JA. Oxidation of p-hydroxybenzoicacid by UV radiation and by TiO 2.UV radiation: comparison and modelling of reaction kinetic. Hazard. Mater. 2001;83: 255–264.

32. Asenjo NG, Santamaría R, Blanco C, Granda M, Álvarez P, Menéndez R. Correct use of the Langmuir–Hinshelwood equation for proving the absence of a synergy effect in the photocatalytic degradation of phenol on a suspended mixture of titania and activated carbon. Carbon. 2013;55:62–69.

33. Leblebici ME, Rongé J, Martens JA, Stefanidis GD, Gerven TV. Computational modelling of a photocatalytic UV-LED reactor with internal mass and photon transfer consideration. Chemical Engineering Journal. 2015;264:962–970.

34. Zhou W, Zhang F, Yuan M, Li B, Peng J, Lv Y, Cai H, Liu X, Chen Q, Dang ZM. Improved dielectric properties and thermal conductivity of PVDF composites filled with core–shell structured Cu@ CuO particles. Materials Science: Materials in Electronics. 2019;30:18350-18361.

35. Walton KS, Snurr RQ. Applicability of the BET method for determining surface areas of microporous metal− organic framework. the American Chemical Society. 2007;129:8552-8556.

36. Barrett EP, Joyner LG, Halenda PP. The determination of pore volume and area distributions in porous substances. I. Computations from nitrogen isotherms. the American Chemical society. 1951;73:373-380.

37. Katsumata H, Oda Y, Kaneco S, Suzuki T. Photocatalytic activity of Ag/CuO/WO 3 under visible-light irradiation. RSC advances. 2013;3:5028-5035.

38. Miyauchi M, Shibuya M, Zhao ZG, Liu Z. Surface wetting behavior of a WO3 electrode under light-irradiated or potential-controlled conditions. The Journal of Physical Chemistry C. 2009;113:10642-10646.

39. RubioLuciano AJ, Soletti LS, CamargoFerreira ME, Cusioli LF, Andrade MB, Bergamasco R, Yamaguchi NU. Manganese ferrite dispersed over graphene sand composite for methylene blue photocatalytic degradation. Journal of Environmental Chemical Engineering. 2020;8:10419.

40. Mohammad Jafri NN, Jaafar J, Alias NH, Samitsu Sh, Aziz F, Wan Salleh WN, Mohd Yusop MZ, Dzarfan Othman MH, Rahman MA, Ismail AF, Matsuura T, Isloor AM. Synthesis and Characterization of Titanium Dioxide Hollow Nanofiber for Photocatalytic Degradation of Methylene Blue Dye. Membranes. 2021;11(8):581.

41. Viet PV, Tran HN. Adsorption and photocatalytic degradation of methylene blue by titanium dioxide nanotubes at different pH conditions. Nanoscience and Nanotechnolog. 2019;10:2043-6254.

42. Samuel MS, Suman S, kannan V, Selvarajan E, Mathimani T, Pugazhendhi A. Immobilization of $Cu_3(btc)_2$ on graphene oxide-chitosan hybrid composite for the adsorption and photocatalytic

degradation of methylene blue. Journal of Photochemistry and Photobiology B: Biology. 2020;204:111809.

43. Deshmukh SP, Kale DP, Kar Sh, Shirsath SR, Bhanvase BA, Saharan VK, Sonawane Sh. Ultrasound assisted preparation of rGO/TiO_2 nanocomposite for effective photocatalytic degradation of methylene blue under sunlight. Nano-Structures & Nano-Objects. 2020;21: 100407.

44. Isai KL, Shrivastava VSh. Photocatalytic degradation of methylene blue using ZnO and 2%Fe–ZnO semiconductor nanomaterials synthesized by sol–gel method: a comparative study. SN Applied Sciencesvolume. 2019;1:1247.

45. Farooq M, Shujah Sh, Tahir K, Hussain ST, Ullah Khan A, Almarhoon ZM, Alabbosh KhF, Alanazi AA, Althagafi TM, Zaki MEA. Phytoassisted synthesis of CuO and Ag–CuO nanocomposite, characterization, chemical sensing of ammonia, degradation of methylene blue. Scientific Reports. 2024;14:1618